Heat diffusion and banding in rapid solidification

Massimo Conti
Dipartimento di Matematica e Fisica, Universitá di Camerino and Istituto Nazionale di Fisica della Materia, 62032 Camerino, Italy
(Received 23 June 1998)

The *banded structures* observed in rapidly solidified alloys originate from an oscillatory dynamics of the solidification front, driven by loss of interfacial equilibrium. To study the formation of these structures, we simulate the rapid directional solidification of a binary alloy with the phase-field model, accounting for both thermal and solute diffusion. We find that the growth process is strongly affected by the interface heating due to the release of latent heat. The interface stability is increased with decreasing the thermal diffusivity D_T, until the oscillatory behavior is suppressed and steady growth occurs. In this respect our results agree with the numerical study of Karma and Sarkissian, based on the diffusional free-boundary model [A. Karma and A. Sarkissian, Phys. Rev. Lett. **27**, 2616 (1992)]. We detect also some deviations whose origin is analyzed and discussed. [S1063-651X(98)03311-X]

PACS number(s): 81.10.Aj, 05.70.Ln, 64.70.Dv

I. INTRODUCTION

Rapid directional solidification allows us to produce a rich variety of metastable phases and microstructures. One of the most interesting effects is the formation, at growth rates near the absolute stability limit, of the so-called *banded structures*. These structures, observed in various aluminum-based alloys obtained using different techniques, consist of alternating light and dark bands lying parallel to the solidification front. The dark bands exhibit a cellular-dendritic or eutectic structure, while the light bands correspond to microsegregation-free regions. The total band spacing ranges from 0.3 to 1.5 μm [1–5]. The physical origin of the banded structures posed an intriguing problem to the scientific community, as they were not expected within the classic Mullins-Sekerka analysis [6]; however, very soon it was realized that departures from local interface equilibrium, neglected in this former approach, could result in a richer behavior of the dynamics of the moving interface. The linear stability analysis of the free-boundary diffusional model was first modified by Coriell and Sekerka [7], who accounted for nonequilibrium solute segregation (''solute trapping'') via a velocity-dependent partition coefficient $k(v)$, defined as the ratio c_s/c_l of the solute concentration in the growing solid to that in the liquid at the interface. Merchant and Davis [8] refined this approach: incorporating into the problem the results of the continuous growth model of Aziz and Kaplan [9], they accounted for both solute trapping and the kinetic undercooling of the moving interface, allowing the segregation coefficient k and the interface temperature T_I to depend on the interface velocity v in a thermodynamically consistent way. Along these lines a new oscillatory instability was identified, characterized by an infinite wavelength along the solid-liquid front; it was argued that this instability should drive the interface dynamics into a nonlinear regime characterized by large oscillations of the interface velocity, reflecting in periodic variations of the solute concentration along the growth direction.

Based on the notion that heat diffusion is much faster than solute diffusion, the above studies used the frozen-temperature approximation, which assumes a uniform temperature gradient, neglecting the latent heat released at the solid-liquid interface. A better understanding of the role of thermal diffusion on the banding phenomena required an extension of the linear stability analysis, which was performed by Huntley and Davis [10]. Karma and Sarkissian [11,12] put further emphasis on this point; in their numerical study, conducted with the Green's-function technique, the picture of the growth process turned out to be strongly altered by the latent heat diffusion. They observed a reduction of the parameters range where the banded structure should occur and a restabilization effect at zero wave number. Moreover, the interface dynamics turned out to be quite insensitive to the external temperature gradient G while, neglecting thermal effects, the band spacing should scale as G^{-1}. Due to the difficulties of evaluating the thermal gradient along the banded structure, no experimental confirmation is available on this point.

All the previous studies addressed the solidification process within the free-boundary diffusional model, imposing on the moving interface boundary conditions derived through a separate modelization of the interface kinetics. Notice that these conditions, based on the results of the continuous growth model, are strictly valid for steady growth [9], and could fail to work during the fast transients characteristic of the banding phenomena. A different approach to investigate the full time-dependent interface dynamics which underlies the bands formation is provided by the phase-field model. Within this method a phase field $\phi(x,t)$ characterizes the phase of the system at each point. A free-energy (or entropy) functional is then constructed that depends on ϕ as well as on the temperature and concentration fields $T,c;a(\nabla\phi)^2$ term accounts for the energy cost associated to the solid-liquid interface. The extremization of the functional with respect to these variables results in the dynamic equations for the process. The model incorporates in a natural fashion nonequilibrium effects as solute trapping and the kinetic undercooling of the moving interface and was previously utilized to simulate the interface dynamics in the frozen-temperature approximation [13,14].

In the present paper the phase-field model will be utilized to investigate the effects of thermal diffusion on the forma-

tion of solute bands. Our results agree in many respects with the picture of the process given by previous studies [10–12] based on the free-boundary formulation of the problem: the interface stability increases with decreasing the thermal diffusivity D_T, until the formation of solute bands is suppressed. However, we detected also some discrepancies: during the fast transients of the process the interface dynamics deviates, to some extent, from the steady-state predictions of the continuous growth model. Moreover, in our study the characteristic thermal length is larger than the system length; as a consequence, the interface heating due to the latent heat release differs from the estimations of Karma and Sarkissian [11,12] and the band spacing scales as G^{-1}.

The paper is organized as follows. In Sec. II the governing equations of the model will be derived, through the extremization of an entropy functional. In Sec. III some details of the numerical method will be given, and in Sec. IV the results of the numerical simulations will be presented and discussed. The conclusions will follow in Sec. V.

II. THE PHASE-FIELD MODEL

The directional solidification of an ideal solution of components A (solvent) and B (solute) is described in terms of the scalar phase field ϕ, the local solute concentration c, and temperature T. The field ϕ is an order parameter assuming the values $\phi=0$ in the solid and $\phi=1$ in the liquid; intermediate values correspond to the interface between the two phases. The model is developed along the lines suggested by Penrose and Fife [15] and successively followed by Wang *et al.* [16], Warren and Boettinger [17], and Conti [18,19]; it incorporates also many of the ideas developed by Caginalp and Xie [20], Caginalp and Jones [21], and Wheeler *et al.* [22,23]. Full details of the derivation are presented elsewhere [14,19], and for the sake of conciseness we shall give below only a short review. As a starting point the entropy of the system is written as

$$\mathcal{S}=\int\left[s(e,\phi,c)-\frac{\epsilon^2}{2}|\nabla\phi|^2\right]dv, \tag{1}$$

where integration is performed over the system volume; the last term in the integrand is a gradient correction to the thermodynamic entropy density s, which depends on the internal energy density e and on the concentration and phase fields through the thermodynamic relations:

$$\frac{\partial s}{\partial e}=\frac{1}{T},\quad \frac{\partial s}{\partial c}=\frac{\mu^A-\mu^B}{T},$$
$$\frac{\partial s}{\partial\phi}=-\frac{1}{T}\frac{\partial}{\partial\phi}[(1-c)\mu^A+c\mu^B], \tag{2}$$

where μ^A and μ^B are the chemical potentials of the solvent and the solute, respectively. Conservation laws govern both solute and energy transport:

$$\dot{c}=-\boldsymbol{\nabla}\cdot\mathbf{J}_c, \tag{3}$$

$$\dot{e}=-\boldsymbol{\nabla}\cdot\mathbf{J}_e. \tag{4}$$

To ensure that the local entropy production is always positive, the solute and energy fluxes can be written in a simple form as

$$\mathbf{J}_c=M_c\boldsymbol{\nabla}\frac{\delta\mathcal{S}}{\delta c}, \tag{5}$$

$$\mathbf{J}_e=M_e\boldsymbol{\nabla}\frac{\delta\mathcal{S}}{\delta e}, \tag{6}$$

while the nonconserved dynamics of the phase field ϕ is expressed through

$$\dot{\phi}=M_\phi\frac{\delta\mathcal{S}}{\delta\phi}, \tag{7}$$

where M_c, M_e, and M_ϕ are positive constants.

Assuming a double well Ginzburg-Landau free energy for the pure constituents, and evaluating the functional derivatives, gives

$$\frac{\partial\phi}{\partial t}=M_\phi[\epsilon^2\boldsymbol{\nabla}^2\phi-(1-c)\tilde{H}^A(\phi,T)-c\tilde{H}^B(\phi,T)], \tag{8}$$

$$\frac{\partial c}{\partial t}=-\boldsymbol{\nabla}\cdot\left\{D_c c(1-c)\frac{v_m}{R}[\tilde{H}^A(\phi,T)-\tilde{H}^B(\phi,T)]\boldsymbol{\nabla}\phi-D_c\boldsymbol{\nabla}c+D_c c(1-c)\frac{v_m}{R}\tilde{\Gamma}(\phi,T)\boldsymbol{\nabla}T\right\}, \tag{9}$$

$$\frac{\partial T}{\partial t}=D_T\boldsymbol{\nabla}^2T-\frac{1}{\chi}[(1-c)L^A+cL^B]\frac{dp(\phi)}{d\phi}\frac{\partial\phi}{\partial t}-\frac{1}{\chi}p(\phi)\times(L^B-L^A)\frac{\partial c}{\partial t}. \tag{10}$$

In Eqs. (8)–(10), R is the gas constant and v_m is the molar volume; the solute diffusivity is defined as $D_c=(M_cR)/[v_mc(1-c)]$ and the thermal diffusivity as $D_T=M_e/(\chi T^2)$, χ being the specific heat, for which we assume equal values for both components in both phases. The function $\tilde{H}^A(\phi,T)$ is defined as

$$\tilde{H}^A(\phi,T)=\frac{dG^A(\phi)}{d\phi}-\frac{dp(\phi)}{d\phi}L^A\frac{T-T^A}{TT^A}, \tag{11}$$

where

$$G^A(\phi)=\tfrac{1}{4}\tilde{W}^A\phi^2(1-\phi)^2=\tilde{W}^Ag(\phi) \tag{12}$$

is a symmetric double-well potential with equal minima at $\phi=0$ and 1, scaled by the positive well height $\tilde{W}^A$; L^A and T^A are the latent heat per unit volume and the melting temperature of the pure component pure A; choosing the function $p(\phi)$ as $p(\phi)=\phi^3(10-15\phi+6\phi^2)$, the condition is enforced that bulk solid and liquid are described by $\phi=0$ and 1, respectively, for every value of temperature [16].

Equations (11) and (12) still hold for $\tilde{H}^B(\phi,T)$ and $G^B(\phi)$ if all the material parameters, labeled with the superscript A, are replaced with the ones related to the B species. The function $\tilde{\Gamma}(\phi,T)$ is defined as

$$\tilde{\Gamma}(\phi,T) = -\frac{p(\phi)}{T^2}\,(L^A - L^B). \tag{13}$$

To allow for different diffusivities in the solid and liquid phases, in the following D_c will be taken as $D_c = D_s + p(\phi)(D_l - D_s)$, and D_l and D_s being the diffusivities in the liquid and in the solid, respectively.

Equations (8)–(10) will be rephrased scaling lengths to some reference length ξ and time to ξ^2/D_l. Allowing M_ϕ to depend on the local composition as $M_\phi = (1-c)M_\phi^A + cM_\phi^B$, and following the lines suggested by Warren and Boettinger [17] to associate the model parameters to the material properties, the governing equations become

$$\frac{\partial \phi}{\partial t} = [(1-c)m^A + cm^B][\nabla^2 \phi + (1-c)Q^A(T,\phi) + cQ^B(T,\phi)], \tag{14}$$

$$\frac{\partial c}{\partial t} = \nabla \cdot \{\lambda(\phi)\nabla c - c(1-c)\lambda(\phi)[H^A(\phi,T) - H^B(\phi,T)]\nabla \phi - c(1-c)\lambda(\phi)\Gamma(\phi,T)\nabla T\}, \tag{15}$$

$$\frac{\partial T}{\partial t} = \frac{1}{\mathrm{Le}}\,\nabla^2 T - \frac{1}{\chi}\,[(1-c)L^A + cL^B]\,\frac{dp(\phi)}{d\phi}\,\frac{\partial \phi}{\partial t} - \frac{1}{\chi}\,p(\phi)(L^B - L^A)\,\frac{\partial c}{\partial t}, \tag{16}$$

where Le is the Lewis number, defined as $\mathrm{Le} = D_l/D_T$, and

$$H^{A,B}(\phi,T) = W^{A,B}\,\frac{dg(\phi)}{d\phi} - L^{A,B}\,\frac{v_m}{R}\,\frac{dp(\phi)}{d\phi}\,\frac{T - T^{A,B}}{TT^{A,B}}$$

$$= \frac{v_m}{R}\,\tilde{H}^{A,B}(\phi,T), \tag{17}$$

$$Q^{A,B}(\phi,T) = -\frac{\xi^2}{(h^{A,B})^2}\,\frac{dg(\phi)}{d\phi} + \frac{1}{6\sqrt{2}}\,\frac{\xi^2 L^{A,B}}{\sigma^{A,B}h^{A,B}}\,\frac{T - T^{A,B}}{\overline{T_I}}\,\frac{dp(\phi)}{d\phi}, \tag{18}$$

$$\Gamma(\phi,T) = \frac{v_m}{R}\,\tilde{\Gamma}(\phi,T), \tag{19}$$

$$\lambda(\phi) = \frac{D_s}{D_l} + p(\phi)\left(1 - \frac{D_s}{D_l}\right). \tag{20}$$

In Eq. (18), $\sigma^{A,B}, h^{A,B}$ indicate the surface tension and the interface thickness of the pure components A and B, respectively; $\overline{T_I}$ is the initial (equilibrium) interface temperature. The model parameters $m^{A,B}, W^{A,B}$ depend on the physical properties of the alloy components through

$$m^{A,B} = \frac{\beta^{A,B}\sigma^{A,B}T^{A,B}}{D_l L^{A,B}}, \quad W^{A,B} = \frac{12}{\sqrt{2}}\,\frac{v_m}{R}\,\frac{\sigma^{A,B}}{T^{A,B}h^{A,B}}, \tag{21}$$

where $\beta^{A,B}$ is the kinetic undercooling coefficient of pure A or B, which relates the interface undercooling to the interface velocity v through $v = \beta^{A,B}(T^{A,B} - T_I)$.

To conduct the numerical simulations we referred to the phase diagram of an ideal solution of nickel (solvent) and copper (solute), using the data summarized in Table I; the solute diffusivity in the solid phase was estimated as $D_s = 10^{-6}D_l$. The length scale was fixed at $\xi = 2.1\times10^{-4}$ cm; the kinetic undercooling coefficients were fixed to $\beta^A = 128.64\ \mathrm{cm\ s^{-1}\ K^{-1}}$ and $\beta^B = 153.60\ \mathrm{cm\ s^{-1}\ K^{-1}}$, not far from the actual best estimates [24] and a realistic value for the interface thickness was selected as 1.68×10^{-7} cm. Using the above values it results $W^A = 0.963$, $W^B = 0.960$, and $m^A = m^B = 350$.

III. THE NUMERICAL METHOD

The evolution of Eqs. (14)–(16) has been considered in one spatial dimension, in the domain $0 \leqslant x \leqslant x_m$, with $x_m = 9.6$. At the domain's boundaries we imposed fluxless conditions for the phase and concentration fields and directional solidification conditions for the thermal field, via

$$\left[\frac{\partial T}{\partial t}\right]_{x=0;x=x_m} = -V_0 G, \tag{22}$$

where G is the external temperature gradient and V_0 is the isotherm velocity. The initial temperature profile was defined as

$$T(x,0) = \overline{T_I} + G(x - x_0) \tag{23}$$

with a phase boundary at temperature $\overline{T_I}$ separating the solid region ($x < x_0$, $\phi = 0$) and the liquid region ($x > x_0$, $\phi = 1$). The initial solute concentration was set to the equilibrium values in the two phases. To discretize the equations second

TABLE I. Material parameters for the Ni-Cu alloy.

	Nickel	Copper
T_m (K)	1728	1358
L (J/cm^3)	2350	1728
v_m (cm^3/mol)[a]	7.0	7.8
σ (J/cm^2)	3.7×10^{-5}	2.9×10^{-5}
D_l (cm^2/s)	10^{-5}	10^{-5}

[a]An average value of 7.4 has been taken.

order in space and first order in time, finite-difference approximations were utilized. Then, an explicit scheme was employed to advance forward in time the phase field and concentration equations; the linear temperature equation was more conveniently integrated with a fully implicit method. To ensure an accurate spatial resolution, the computational domain was divided into two parts; in an inner region, ($4.0 \leqslant x \leqslant 5.6$) concerned with the evolution of the phase and concentration fields, the grid spacing was selected as $\Delta x_i = 4 \times 10^{-4}$, which is one-half the nominal interface thickness; in the outer region ($0 \leqslant x \leqslant 4.0$; $5.6 \leqslant x \leqslant 9.6$) only the more diffuse temperature field changes with time; here a grid spacing $\Delta x_0 = 10 \Delta x_i$ was utilized. A time step $\Delta t = 2 \times 10^{-10}$ was required for numerical stability. To verify the consistency of the numerical scheme, at each time step the solute conservation was checked and in all the simulations it was verified within 0.001%.

IV. NUMERICAL RESULTS

The solidification process is characterized by the constitutional laws $T_I(v), k(v)$ which relate the interface temperature and the partition coefficient to the interface velocity. The steady $T_I(v)$ curve exhibits a nonmonotonic behavior: due to suppression of solute partitioning (and to the reduction of solute concentration on the liquid side of the interface), at low velocities $T_I(v)$ first rises, then falls with increasing v reflecting the increasing undercooling required to advance the solidification front. The loss of interface stability is expected when the isotherm velocity is fixed in the region of positive slope of the $T_I(v)$ curve, corresponding to the unstable planar growth branch. Setting the solute concentration in the liquid phase at $c_{+\infty} = 0.070\,68$, $T_I(v)$ reaches its maximum at $v = 1350$ [13] (here and in the following, except for temperatures, physical quantities will be expressed in dimensionless units). Then we chose an isotherm velocity $V_0 = 700$, well inside the unstable branch; the external temperature gradient was fixed at $G = 40$ K.

The high value of the Lewis number ($\mathrm{Le} = 5 \times 10^{-5}$) prevents the formation of the banded structures in the Ni-Cu alloy, forcing steady growth for every value of the isotherm velocity or the external temperature gradient. Then we artificially altered the thermal diffusivity of the alloy by a factor $\sim 10^2$, entering the region where the crossover from the steady to the oscillatory dynamics of the solidification front can be studied. With this choice the thermal diffusion length $1/(\mathrm{Le} V_0)$ turns out to be much larger than the domain's size; in this respect our simulations explore the opposite limit of the growth conditions studied by Karma and Sarkissian [11,12], who assumed an infinite domain. Notice that in actual rapid solidification experiments the domain's size and the thermal diffusion length are of the same order [3].

The effect of heat diffusion on the growth dynamics is shown in Figs. 1(a)–1(c), where plots of interface velocity and temperature versus time are presented for three different values of the Lewis number. Figure 1(a) refers to the frozen temperature approximation ($\mathrm{Le} = 0, D_T = \infty$); after a short transient the initial conditions are reabsorbed and the front velocity enters an oscillatory regime around the average value V_0. Most of the time is spent at low velocity, where $v < V_0$ and the interface cools down. The high velocity por-

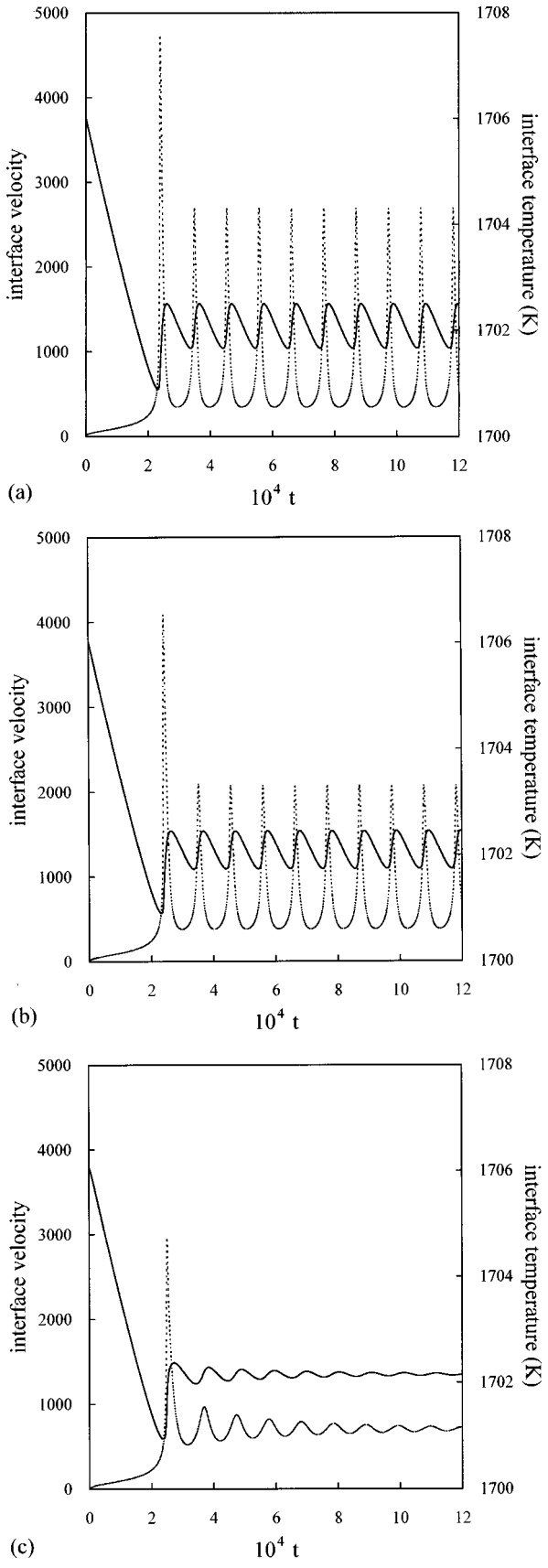

FIG. 1. Interface velocity (dotted line) and temperature (solid line) versus time. The Lewis number is (a) $\mathrm{Le} = 0$, (b) $\mathrm{Le} = 6.65 \times 10^{-8}$, and (c) $\mathrm{Le} = 3.12 \times 10^{-7}$. The isotherm velocity is $V_0 = 700$ and the temperature gradient $G = 40$ K.

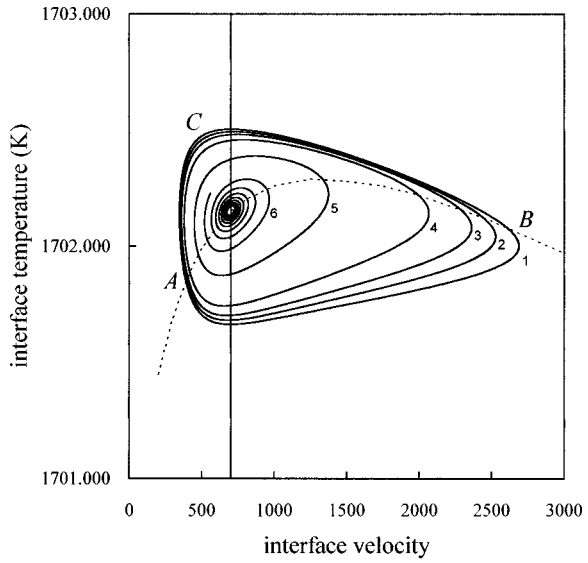

FIG. 2. Cycles described by the process in the (T_I,v) plane. The curves refer to increasing values of the Lewis number: in the order 1 to 6 we have Le$=0$, 1.65×10^{-8}, 3.30×10^{-8}, 6.60×10^{-8}, 1.65×10^{-7}, and 3.12×10^{-7}, respectively. The isotherm velocity is $V_0=700$ and the temperature gradient $G=40$ K. The vertical line indicates the isotherm velocity V_0; the meaning of points *A,B,C* is illustrated in the text.

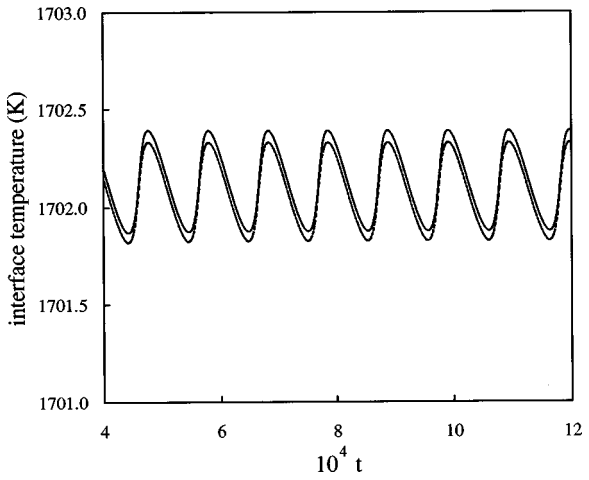

FIG. 3. Interface temperature versus time (solid line). The dashed line is drawn using the estimation given by Eq. (25). The isotherm velocity is $V_0=700$ and the temperature gradient $G=40$ K. The Lewis number is Le$=1.65\times10^{-7}$.

tion of the cycle ($v>V_0$) occurs on a much shorter time scale, marked by the sharp peaks of the $v(t)$ curve. In Fig. 1(b), the Lewis number is Le$=6.65\times10^{-8}$; the finite thermal diffusivity is reflected in the decrease of the maximum velocity reached during the fast growth stage. A much more dramatical effect is observed in Fig. 1(c), where Le$=3.12\times10^{-7}$: the amplitude of the oscillations decreases with time, until an asymptotical steady regime is reached.

The origin of this effect can be understood looking at Fig. 2, where we have compared the orbits described by the system in the (T_I,v) plane with different values of the Lewis number (increasing in the order 1–6). The vertical line indicates the isotherm velocity $V_0=700$; on the same graph the dashed line is the steady $T_I(v)$ curve. Curve 1 refers to the frozen temperature approximation; for most of the cycle the interface velocity is lower than V_0 and the interface cools down; then the orbit traverses the steady $T_I(v)$ curve at point *A* and with a strong acceleration reaches point *B* on the stable branch. Here the interface velocity is much higher than V_0 and the interface warms up; solidification is decelerated and the operating point shifts to *C*. When the frozen temperature approximation is relaxed, the excess of latent heat released at the interface during acceleration has to be removed through thermal diffusion; the mechanism becomes less effective with decreasing the thermal diffusivity D_T, reflecting in an increased temperature of the interface. The effect is clearly recognizable in curves from 2 to 5, where the slope of the $T_I(v)$ trajectories increases upwards during acceleration with increasing the Lewis number. Correspondingly, the operating point on the stable branch shifts from *B* and approaches the maximum of the steady $T_I(v)$ curve. When Le$=3.12\times10^{-7}$ the trajectory (curve 6) no longer reaches the stable branch, and collapses into a single point at velocity V_0.

The quantitative effects of the latent heat diffusion can be assessed through a simple argument. As we previously mentioned, in our system the thermal diffusion length is much larger than the domain's size. Then, assuming linear temperature profiles, energy conservation at the interface requires

$$\frac{T_I-T_1}{x_I}=\frac{T_2-T_I}{x_m-x_I}+\frac{L}{\chi}v\,\mathrm{Le}, \tag{24}$$

where $T_1=T(x=0;t)$, $T_2=T(x=x_m;t)$, and x_I is the x coordinate of the solidification front. The latent heat of the alloy is indicated here with L. After a simple manipulation Eq. (24) gives the interface temperature as

$$T_I=\frac{1}{x_m}\left[T_1(x_m-x_I)+T_2x_I\right]+\frac{x_I(x_m-x_I)}{x_m}\frac{L}{\chi}v\,\mathrm{Le}. \tag{25}$$

The first term on the right-hand side of Eq. (25) gives the contribution to T_I due to the external temperature profile; the second term is the overheating due to the latent heat released at the interface. We observe in Fig. 2 that a temperature jump of a few tenths of a degree during the accelerating part of the cycle is enough to prevent a stable oscillatory regime. As in our system $x_I(x_m-x_I)/x_m\sim x_m/4$ and $v\sim10^3$, we see from Eq. (25) that the crossover between the oscillatory and the steady regime should be expected with the Lewis number ranging from 1×10^{-7} to 5×10^{-7}. To verify the consistency of the above arguments, in Fig. 3 we represent versus time the actual interface temperature (solid line) and the estimation given by Eq. (25) (dashed line). For clarity we omitted the initial transient. It can be observed that the agreement between the two curves is quite satisfactory. We note also that the latent heat contribution to the interface heating scales approximately as $\sim x_m\mathrm{Le}$; then we expect that the interface dynamics should depend on the thermal diffusivity and the system size only through the product $x_m\mathrm{Le}$. This suggestion is confirmed in Fig. 4, where the solid line represents the

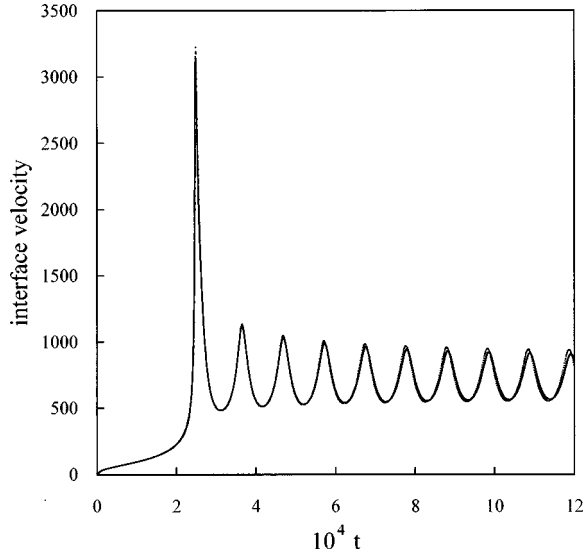

FIG. 4. Interface velocity versus time, for two different values of the Lewis number and the domain's size. Solid line: $\mathrm{Le}=2.5\times10^{-7}$; the dashed line is drawn for $\mathrm{Le}=2\times10^{-7}$. In both cases $x_m\mathrm{Le}=24$; The isotherm velocity is $V_0=700$ and the temperature gradient $G=40$ K.

time variation of the interface velocity for $\mathrm{Le}=2.5\times10^{-7}$; the dashed line is drawn for $\mathrm{Le}=2\times10^{-7}$. In both cases $x_m\mathrm{Le}=24$; we can observe that the two curves are almost indistinguishable.

Karma and Sarkissian [11,12], considering an infinite domain, found that the growth process is essentially driven by the interface overheating caused by the release of latent heat, and is almost independent of the external temperature gradient. In contrast, in the frozen temperature approximation, estimates based on the continuous growth model indicate that the oscillation frequency should scale as $\sim G$ and the band spacing as $\sim G^{-1}$. Due to the small domain's size, in our simulations the interface temperature is very sensitive to

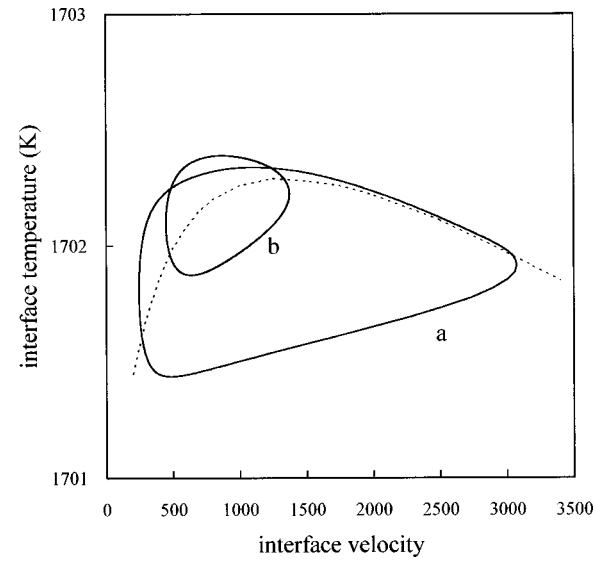

FIG. 5. Effect of the external gradient G on the cycles described by the process in the (T_I,v) plane. Curve (a): $G=10$ K; curve (b) is drawn for $G=40$ K. The Lewis number is $\mathrm{Le}=1.65\times10^{-7}$ and the isotherm velocity is $V_0=700$.

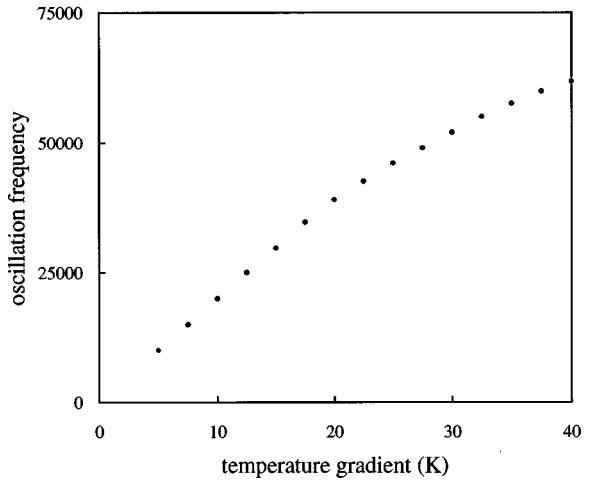

FIG. 6. Oscillation frequency versus the external gradient G. The Lewis number is $\mathrm{Le}=1.65\times10^{-7}$ and the isotherm velocity is $V_0=700$.

the boundary conditions imposed at the domain's walls, and the external gradient plays a central role in controlling the interface dynamics. In Fig. 5 we show, in the T,v plane, the cycles computed with $G=10$ K (curve a) and $G=40$ K (curve b). The larger slope of curve b during the acceleration period indicates that the motion in the external gradient contributes to a large extent to the heating of the interface; as a consequence the amplitude of the oscillations decreases with increasing G. In Fig. 6 the oscillation frequency ω is represented versus G; we observe that ω is an increasing function of G, and at low frequencies scales approximately as $\sim G$.

The low frequency of the oscillations for small values of G accounts for the fact that during the high velocity section of the cycle the trajectory (a) in Fig. 5 follows very closely the steady $T_I(v)$ curve. As the solute relaxation across the interface is not instantaneous, at high frequency the steady approximation fails to work [curve (b)]. This issue has been discussed in more detail elsewhere [14].

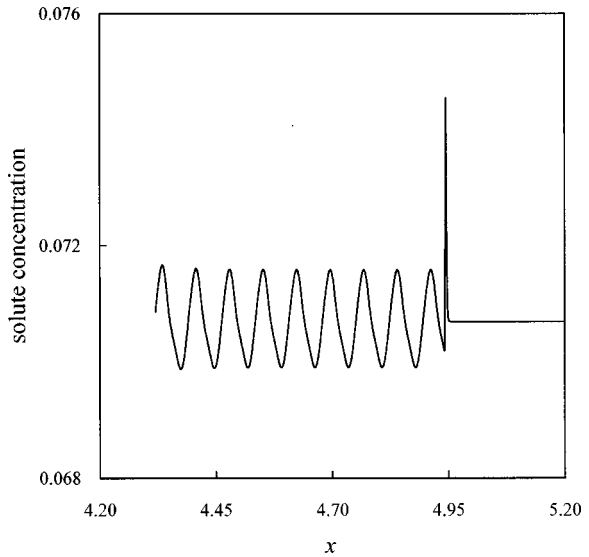

FIG. 7. Solute concentration profile along the growth direction. The isotherm velocity is $V_0=700$, and the temperature gradient is $G=40$ K. The Lewis number is $\mathrm{Le}=1.65\times10^{-7}$.

In Fig. 7 the concentration profile is shown for $G=40$ K, $\mathrm{Le}=1.65\times10^{-7}$. We observe that the oscillatory dynamics of the solidification front is reflected in a periodic structure of the solidified alloy. The wavelength of the banded structure has been estimated as $\lambda=0.0720$, which is practically coincident with the expected value $2\pi V_0/\omega=0.0721$.

V. CONCLUSIONS

In summary, we addressed rapid directional solidification using a phase-field model which accounts for both solute and thermal diffusion. In a region of the parameters space, the interface dynamics enters an oscillatory regime characterized by periodic variations of the growth rate. The growth process is strongly affected by the interface heating due to the release of latent heat. According to previous results based on the free-boundary model, the interface stability is increased with decreasing the thermal diffusivity D_T, until the oscillatory behavior is suppressed and steady growth occurs. When the thermal diffusion length is much larger than the domain's size, the interface heating differs from the estimations of Karma and Sarkissian [11,12]: in this limit the role of the external temperature gradient cannot be neglected and the oscillation frequency scales as $\sim G$. At low frequency, the interface conditions provided by the continuous growth model describe to a good degree of accuracy the actual interface dynamics; at high frequency, due to the fast transients involved, these conditions no longer work, and the results of the phase-field simulations deviate, to some extent, from the predictions of the free-boundary model.

[1] M. Zimmermann, M. Carrard, and W. Kurz, Acta Metall. **37**, 3305 (1989).
[2] M. Zimmermann, M. Carrard, M. Gremaud, and W. Kurz, Mater. Sci. Eng., A **134**, 1278 (1991).
[3] M. Gremaud, M. Carrard, and W. Kurz, Acta Metall. Mater. **39**, 1431 (1991).
[4] W. J. Boettinger, D. Shechtman, R. J. Schaefer, and F. S. Biancaniello, Metall. Trans. A **15**, 55 (1984).
[5] M. Carrard, M. Gremaud, M. Zimmermann, and W. Kurz, Acta Metall. Mater. **40**, 983 (1992).
[6] W. W. Mullins and R. F. Sekerka, J. Appl. Phys. **35**, 444 (1964).
[7] S. R. Coriell and R. F. Sekerka, J. Cryst. Growth **61**, 499 (1983).
[8] G. J. Merchant and S. H. Davis, Acta Metall. Mater. **38**, 2683 (1990).
[9] M. J. Aziz and T. Kaplan, Acta Metall. **36**, 2335 (1988).
[10] D. A. Huntley and S. H. Davis, Acta Metall. Mater. **41**, 2025 (1993).
[11] A. Karma and A. Sarkissian, Phys. Rev. Lett. **27**, 2616 (1992).
[12] A. Karma and A. Sarkissian, Phys. Rev. E **47**, 513 (1993).
[13] M. Conti, Phys. Rev. E **56**, R6267 (1997).
[14] M. Conti (unpublished).
[15] O. Penrose and P. C. Fife, Physica D **43**, 44 (1990).
[16] S. L. Wang, R. F. Sekerka, A. A. Wheeler, B. T. Murray, S. R. Coriell, R. J. Braun, and G. B. McFadden, Physica D **69**, 189 (1993).
[17] J. A. Warren and W. J. Boettinger, Acta Metall. Mater. **43**, 689 (1995).
[18] M. Conti, Phys. Rev. E **55**, 701 (1997).
[19] M. Conti, Phys. Rev. E **55**, 765 (1997).
[20] G. Caginalp and W. Xie, Phys. Rev. E **48**, 1897 (1993).
[21] G. Caginalp and J. Jones, Ann. Phys. (N.Y.) **237**, 66 (1995).
[22] A. A. Wheeler, W. J. Boettinger, and G. B. McFadden, Phys. Rev. A **45**, 7424 (1992).
[23] A. A. Wheeler, W. J. Boettinger, and G. B. McFadden, Phys. Rev. E **47**, 1893 (1993).
[24] R. Willnecker, D. M. Herlach, and B. Feuerbacher, Phys. Rev. Lett. **62**, 2707 (1989).